Environmental Science & Technology

Article

pubs.acs.org/est

Uranium Bioreduction Rates across Scales: Biogeochemical Hot Moments and Hot Spots during a Biostimulation Experiment at Rifle, Colorado

Chen Bao,[†] Hongfei Wu,[†] Li Li,[*,†,‡,§] Darrell Newcomer,[∥] Philip E. Long,[⊥] and Kenneth H. Williams[⊥]

[†]John and Willie Leone Department of Energy and Mineral Engineering, [‡]EMS Energy Institute, and [§]Earth and Environmental Systems Institute (EESI), Pennsylvania State University, University Park, Pennsylvania 16802, United States

[∥]Pacific Northwest National Laboratory, Richland, Washington 99352, United States

[⊥]Lawrence Berkeley National Laboratory, 1 Cyclotron Road, Berkeley, California 94701, United States

Supporting Information

ABSTRACT: We aim to understand the scale-dependent evolution of uranium bioreduction during a field experiment at a former uranium mill site near Rifle, Colorado. Acetate was injected to stimulate Fe-reducing bacteria (FeRB) and to immobilize aqueous U(VI) to insoluble U(IV). Bicarbonate was coinjected in half of the domain to mobilize sorbed U(VI). We used reactive transport modeling to integrate hydraulic and geochemical data and to quantify rates at the grid block (0.25 m) and experimental field scale (tens of meters). Although local rates varied by orders of magnitude in conjunction with biostimulation fronts propagating downstream, field-scale rates were dominated by those orders of magnitude higher rates at a few selected hot spots where Fe(III), U(VI), and FeRB were at their maxima in the vicinity of the injection wells. At particular locations, the hot moments with maximum rates negatively corresponded to their distance from the injection wells. Although bicarbonate injection enhanced local rates near the injection wells by a maximum of 39.4%, its effect at the field scale was limited to a maximum of 10.0%. We propose a rate-versus-measurement-length relationship ($\log R' = -0.63 \log L - 2.20$, with R' in μmol/mg cell protein/day and L in meters) for orders-of-magnitude estimation of uranium bioreduction rates across scales.

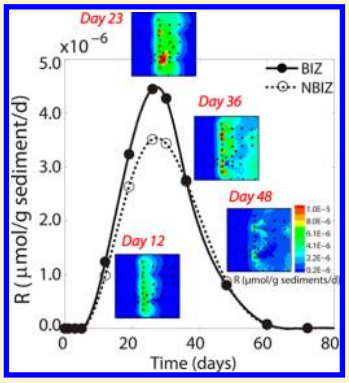

INTRODUCTION

Uranium is a common contaminant and can exist in highly soluble form as U(VI) or as sparingly soluble U(IV) in subsurface environments.[1,2] The microbe-mediated reduction of U(VI) to U(IV) can immobilize U(VI) and therefore mitigate its further migration.[3] Rates of uranium bioreduction have been measured extensively in laboratory systems and have been reported to depend on various biogeochemical factors, including concentration and types of inhibitors,[4,5] ligands,[6,7] electron acceptors and donors,[3,8−11] and bacterial species.[3,12]

In natural soils and sediments, chemical species undergo complicated hydrological, geochemical, and biogeochemical processes.[13−15] Biogeochemical reaction rates at any particular local location are dictated by the local (bio)geochemistry, including the availabilities of electron donors, acceptors, and competitors, which in turn depend on the flow and transport processes.[4,16−18] At larger scales, the rates are collectively determined by the local rates and depend on the distribution of physical and geochemical properties such as porosity, permeability, and mineral composition.[19,20] In comparison to laboratory work, fewer studies have examined the controlling factors that determine field scale rates.[21−25] One consistent observation has been that field-scale rates are significantly lower than those measured in laboratories. For example, the uranium bioreduction rate of 1 μmol of U(VI)/mg biomass/day has been reported in a field experiment,[26] while its corresponding laboratory rate with the same culture has been reported to be 43.2 μmol of U(VI)/mg biomass/day.[27] Spatial patterns of subsurface properties that enhance contact among reactants have been observed to lead to higher field-scale bioreduction rates.[28] However, in general, we do not fully understand key controls of field-scale rates.

U(VI) can exist in the aqueous phase and sorb to solid substrates (both mineral and biopolymer) as U(VI).[14] Bicarbonate has been shown to be effective in desorbing U(VI) from sediments in laboratory experiments[29−31] and at the field scale.[32,33] The potential coupling of bioreductive immobilization and bicarbonate-induced desorption of U(VI) raises a series of intriguing questions. Can bicarbonate-induced desorption enhance U(VI) bioreduction at the field scale? How do bioreduction rates propagate over time and across scales? What are the key controls at the field scale?

Here we answer these questions using the 2010 biostimulation experiment at the U.S. Department of Energy (DOE) Integrated Field Research Challenge (IFRC) site near Rifle,

Received: August 20, 2013
Revised: July 9, 2014
Accepted: July 31, 2014
Published: July 31, 2014

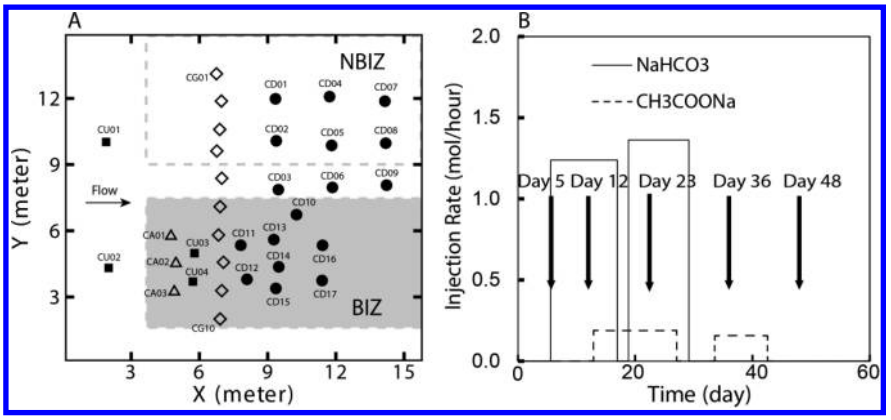

Figure 1. (A) Well layout for the 2010 Rifle field experiment. The wells include background wells (filled squares, CU01−CU04), bicarbonate injection wells (open triangles, CA01−CA03), acetate/bromide injection wells (open diamonds, CG01−CG10), and monitoring wells (filled circles, CD01−CD17). The gray area indicates the approximate bicarbonate injection zone (BIZ) that is the direct down gradient of the bicarbonate injection wells CA01−CA03. The white area within the dashed line stands for no bicarbonate injection zone (NBIZ). (B) Schedule and rates of bicarbonate injection (solid line) and acetate/bromide injection (dashed line) during the experiments. Arrows indicate the days (0, 12, 23, 36, and 48) when spatial profiles of key species are plotted later on. Sodium bicarbonate injection started on day 5, with a stop between days 17 and 19, and resumed until day 29. It was injected at a tank concentration of 0.05 mol/L, with an injection rate targeting a 2-fold decrease in concentration upon aquifer amendment. Its injection started before acetate injection so as to mobilize the adsorbed U(VI) for bioreduction. A mixture of sodium acetate (0.05 mol/L) and sodium bromide (0.02 mol/L) was injected from day 13 to 27, which overlapped with the bicarbonate injection. The second acetate injection was from day 33 to 43, when the bicarbonate injection ended.

Colorado (USA). The Rifle site was formerly a uranium ore processing facility and is contaminated with uranium at the micromolar level. Multiple biostimulation experiments have been performed at the site.[21,34−36] Although uranium has been observed to be reduced by sulfate-reducing bacteria (SRB) at other sites,[18] at the Rifle site it has been found to primarily result from the enzymatic activity of Fe-reducing bacteria (FeRB)[34,35] and to a lesser extent its interactions with reduced sulfur species.[37] During the 2010 experiment, acetate was injected into the whole experimental domain to stimulate the uranium bioreduction while bicarbonate was injected into half of the domain to evaluate its effect on enhancing bioreduction at the field scale. The hydrological and aqueous geochemistry field data were integrated using a reactive transport model to understand the temporal and spatial evolution of bioreduction from the grid block scale (0.25 m) to the field domain (tens of meters).

MATERIALS AND METHODS

Rifle Integrated Field Research Challenge (IFRC) Site and the 2010 Field Experiment. Comprehensive descriptions of the Rifle site have been presented elsewhere.[21,34,35,38] Briefly, shallow groundwater at the site is contaminated with uranium at a concentration of 0.2−1.5 μM, which is higher than the U.S. Environmental Protection Agency's (EPA) drinking water standard (0.126 μM). Important aqueous species include calcium, magnesium, chloride, sulfate, and bicarbonate, as given in Table S1 (Supporting Information). The sediments include both gravels and cobbles as coarse-grained materials and fine-grained silt and clay. The minerals include quartz, calcite, clays, and various iron-containing minerals (goethite, hematite, and magnetite).[39]

The 2010 experiment combined bicarbonate amendment for U(VI) desorption and acetate amendment for U(VI) bioreduction.[40] The well map and injection history are shown in Figure 1. As evidenced by the appearance of the conservative tracer deuterium (data not shown), the impact of the bicarbonate injection was primarily in the region down gradient of the injection wells (gray zone in Figure 1), hereafter referred to as the "bicarbonate injection zone" (BIZ), in contrast to the "no bicarbonate injection zone" (NBIZ). Prior to the amendment, slug tests were conducted to measure the hydraulic conductivity. Groundwater samples were collected during the experiment for the analysis of aqueous composition. These data served as constraints for the reactive transport model.

Overview of the Model Integration Method. The integration method involves using data from slug tests and a geostatistical method to obtain an initial distribution of hydraulic conductivity, a probability model that inversely correlates hydraulic conductivity and the initial "bioavailable" Fe(III) spatial distribution. Inverse reactive transport modeling was carried out to determine the controlling parameters that best fit the tracer and geochemical breakthrough data in multiple wells. After that the spatiotemporal evolution of aqueous and solid species were generated to understand the processes at different spatial scales from the local grid block scale of 0.25 m to the scale of the domain at approximately 10 m.

Spatial Distribution of Hydraulic Conductivity and Fe(III) Content. Hydraulic conductivity was measured at 26 locations using slug tests[41] and varied more than 1 order of magnitude, with a maximum of 21.6 m/d at CG05 and a minimum of 0.9 m/d at CD02. To obtain values for locations without data, krigging was performed using Tecplot (Tecplot, Inc.). For each point without data, the hydraulic conductivity was calculated from a weighted linear combination of the source data, taking into account all 26 data points.[42−44] Details of the krigging method and the original hydraulic conductivity data are in Table S2 (Supporting Information).

The bioavailable iron content is important because Fe-reducing bacteria are believed to be the primary agents of enzymatic U(VI) reduction following acetate injection at the Rifle site.[45] As suggested by detailed analysis, Fe(III) phases in Rifle sediments include Fe oxides, with a substantial proportion being goethite and small percentages (~5%) of ferrihydrite.[39]

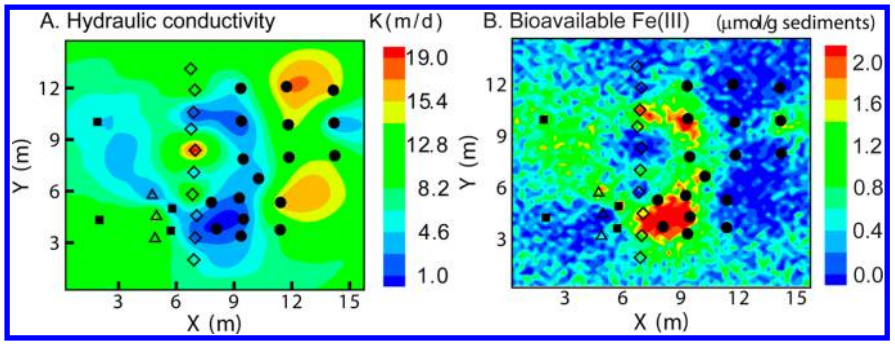

Figure 2. Initial spatial distribution of (A) hydraulic conductivity (m/d) inferred from measured data and (B) bioavailable Fe(III) content (μmol/g sediments) obtained by using average bioavailable iron content and a negative correlation with hydraulic conductivity. Also shown are background wells (filled squares), bicarbonate injection wells (open triangles), acetate/bromide injection wells (open diamonds), and monitoring wells (filled circles). The hydraulic conductivity and bioavailable Fe(III) show an inverse pattern, as assumed in the probability model.

The Fe(III) phases were observed to closely associate with low-permeability clay-rich samples. As such, we assumed a negative correlation between the iron content and hydraulic conductivity and used goethite as the representing Fe(III) mineral in Fe-bioreduction reaction. As has been done in previous studies,[24] the initial distribution of the bioavailable Fe(III) was determined on the basis of the distribution of hydraulic conductivity and a probability model (Supporting Information). The Fe(III) content used here, however, represents the total of "all" bioavailable forms, not just goethite. Similarly, the Fe(III) bioreduction rate reflects more the "average" rates of all Fe(III) minerals instead of just goethite. The bioavailable Fe(III) distribution in Figure 2 exhibits an inverse pattern of hydraulic conductivity, as expected from their negative correlation.

Reactive Transport Modeling (RTM). The coupled fluid flow, mass transport, and biogeochemical processes were simulated using the widely used reactive transport code CrunchFlow in various earth and environmental science applications.[46−48] CrunchFlow partitions aqueous species into primary and secondary species.[49] The primary species constitutes a critical set of species upon which the concentrations of secondary species can be written through the mass action laws of instantaneous reactions. The mass conservation equations together with the laws of mass action were solved for the spatiotemporal evolution of all species.[50] A typical mass conservation equation for a primary species j is written as

$$\frac{\partial(\phi C_j)}{\partial t} = \nabla\bullet(\boldsymbol{D}\nabla(\phi C_j) - \boldsymbol{u}C_j) - \sum_{r=1}^{N_r} v_{jr}R_r - \sum_{m=1}^{N_m} v_{jm}R_m \quad (1)$$

Here ϕ is porosity (m^3 of water/m^3 porous media), C_j is the aqueous concentration (mol/m^3 water), $\boldsymbol{D}$ is the diffusion/dispersion coefficient (m^2/s), $\boldsymbol{u}$ is the Darcy flux that is equal to the product of porosity and flow velocity (m/s), N_r is the total number of kinetic aqueous reactions that involve j, v_{jr} is the stoichiometric coefficient of j associated with the reaction r, R_r is the rate of aqueous reaction r (mol/m^3 porous media/s), N_m is the total number of kinetic mineral reactions that involve species j, v_{jm} is the stoichiometric coefficient of j in reaction m, and R_m is the rate of mineral reaction m (mol/m^3 porous media/s). This equation explicitly includes the diffusion/dispersion, advection, and multiple reactions and can differentiate the contribution of individual processes. A total of 23 equations were solved for the 23 primary species, with another 52 secondary species calculated on the basis of the laws of mass action (Table S3, Supporting Information).

Complex biogeochemical reactions occurred during the biostimulation experiments. The driving forces of the system are the microbe-mediated bioreduction of Fe(III), U(VI), and sulfate.[34,36,51] Using bacterial energetics as outlined in Rittmann and McCarty,[51] these reactions are written as

$$\mathrm{FeOOH(s) + 1.92H^+ + 0.033NH_4^+ + 0.208CH_3COO^- \rightarrow Fe^{2+} + 0.033C_5H_7O_2N_{(FeRB)} + 0.250HCO_3^- + 1.600H_2O} \quad (2)$$

$$\mathrm{SO_4^{2-} + 1.082CH_3COO^- + 0.052H^+ + 0.035NH_4^+ \rightarrow 0.035C_5H_7O_2N_{(SRB)} + 0.104H_2O + 2HCO_3^- + HS^-} \quad (3)$$

$$\mathrm{UO_2^{2+} + 0.067NH_4^+ + 0.417CH_3COO^- + 0.8H_2O \rightarrow UO_2(s) + 0.067C_5H_7O_2N_{(FeRB)} + 0.5HCO_3^- + 2.15H^+} \quad (4)$$

In these equations, $C_5H_7O_2N_{(FeRB)}$ and $C_5H_7O_2N_{(SRB)}$ represent the biomasses of FeRB and SRB, respectively. The yield coefficient of a specific bacterium can vary by an order of magnitude, depending on the growing conditions.[51,52] The typical range is 0.03−0.57 mol of biomass/mol substrate for Geobacteraceae.[52−55] Here we chose 0.16 and 0.03 mol biomass/mol substrate for FeRB and SRB, respectively, to be consistent with literature values.[56] At the micromolar level, uranium toxicity was considered negligible and its bioreduction followed the Monod model,[57] similar to those of Fe(III) and sulfate:[58,59]

$$R_{Fe(III)} = -k_{max,Fe(III)}X_{FeRB}\frac{C_{acetate}}{K_{M,acetate} + C_{acetate}} \times \frac{C_{Fe(III)}}{K_{M,Fe(III)} + C_{Fe(III)}} \quad (5)$$

$$R_{sulfate} = -k_{max,sulfate}X_{SRB}\frac{C_{acetate}}{K_{M,acetate} + C_{acetate}} \times \frac{C_{sulfate}}{K_{M,sulfate} + C_{sulfate}}\frac{K_{I,Fe(III)}}{K_{I,Fe(III)} + C_{Fe(III)}} \quad (6)$$

$$R_{U(VI)} = -k_{max,U(VI)} X_{FeRB} \frac{C_{acetate}}{K_{M,acetate} + C_{acetate}} \times \frac{C_{U(VI)}}{K_{M,U(VI)} + C_{U(VI)}} \quad (7)$$

Here each rate depends on the maximum rate constant k_{max} (mol/(L/s/cell)), the amount of bacteria X_{FeRB} and X_{SRB} (cells), and the concentrations (mol/L) of the electron donor acetate $C_{acetate}$ and acceptor (TEA) through the dual Monod terms with their respective half-saturation constants $K_{M,acetate}$ and $K_{M,TEA}$ (mol/L). Sulfate reduction was assumed to be inhibited by Fe(III) oxides through the inhibition term because of the lower energy yield from sulfate reduction in comparison to that of Fe(III) reduction.[60−62] At the Rifle site, with acetate being the electron donor, uranium bioreduction largely depends on Fe-reducing bacteria, which in turn depends on local concentrations of Fe(III)-containing minerals and acetate. Existing work has shown that inhibition of U(VI) bioreduction by Fe(III) occurs when ferrihydrite is the abundant Fe(III) mineral and when the U(VI) concentration is relatively high.[63] At the Rifle site, ferrihydrite only occupies a small percentage (~5%) of Fe(III) minerals[39] and the U(VI) concentration is at the micromolar level, 3 orders of magnitude lower than the lowest concentration used in experiments where the inhibition effects were observed. As such, inhibition of U(VI) bioreduction by Fe(III) was not included. In addition, U(VI) and Fe(III) bioreduction were observed to occur concomitantly at the Rifle site.[34] The abiotic reductions of U(VI) and Fe(III) by sorbed Fe(II) species[64−66] were not included because these reactions were found to be negligible in natural sediments, especially in those with low Fe content (1−5 wt % of Fe),[66−68] which is the case at Rifle.

The products of microbe-mediated reactions lead to mineral dissolution and precipitation and aqueous speciation reactions. The injectates also induce reactions including surface complexation, ion exchange, and aqueous speciation. Details of the reactions, kinetic rate laws, and thermodynamic information are documented in Table S4 (Supporting Information). All other aqueous speciation reactions are detailed in Tables S5 and S6 (Supporting Information). In total, 75 species and 69 reactions were included.

Numerical Procedure. Two-dimensional simulations were carried out within a 16 m × 15 m square domain, with a total of 3840 (64 × 60) grid blocks and a resolution of 0.25 m × 0.25 m. The flow field was calculated using the distribution of hydraulic conductivity and a constant pressure gradient that gave an average flow velocity of approximately 0.30 m/d as reported for the Rifle site.[34,69] Permeability values were updated every time step on the basis of the porosity alteration resulting from biomass growth and mineral reactions. However, the porosity alteration on the order of 0.002 had negligible effects on hydraulic conductivity due to the relatively short duration of acetate injection. A dispersivity value of 0.20 m sufficiently reproduced the bromide data through inverse transport modeling.

Measured background concentrations were used as the initial and boundary conditions (Table S1, Supporting Information). We explicitly modeled the growth of the microbial communities FeRB and SRB, according to reactions 2−4. Bacteria were assumed immobile because the majority of the cells were observed to attach to the sediments either in the form of biofilms or as separate microbial colonies.[51,70,71] Both FeRB and SRB were considered to exist ubiquitously initially, occupying 10^{-4} solid volume percentage. This corresponds to a cell density between 3×10^5 and 9×10^6 cells/mL the sediment [Dr. Aaron Peacock, personal communication], within the typically reported cell density range of 10^4−10^7 cells/mL of the sediment.

Average Uranium Bioreduction Rates. The local grid block scale rates were directly calculated from the RTM. At the intermediate and field scale, precipitated U(IV) (μmol/g sediment) was used to estimate the bioreduction rates according to eq 8:

$$\overline{C_{U(IV),t_j}} = \frac{\frac{1}{M_{w,U(IV)}} \sum_{i=1}^{N} \phi_{U(IV),i,t_j} \rho_{U(IV)}}{\sum_{i=1}^{N} (1 - \phi_{i,t_j}) \rho_{sediment}}$$

$$R_{U(IV),t_j} = \frac{\overline{C_{U(IV),t_{j+1}}} - \overline{C_{U(IV),t_j}}}{t_{j+1} - t_j} \quad (8)$$

where N is the number of grid blocks within the area of interest, t_j is the specific time, $\phi_{U(IV),i,t_j}$ and ϕ_{i,t_j} (volume/total porous medium volume) are the volume fractions of precipitated U(IV) (in the form of uraninite UO_2(s)) and porosity in the grid block i at time t_j, respectively, and $\rho_{U(IV)}$, $M_{W,U(IV)}$, and $\rho_{sediment}$ are the density (10.97 g/cm^3) and molecular weight of uraninite (270.03 g/mol), and sediment density (2.65 g/cm^3), respectively. Therefore, $\overline{C_{U(IV),t_j}}$ is the solid U(IV) concentration averaged over the area of interest (mol/g sediment) at time t_j. $R_{U(IV),t_j}$ is the corresponding averaged rate of U(VI) bioreduction (mol of U(VI)/g sediment/day). Because the rates also depend on the amount of biomass, we alternatively calculate the rates normalized by the FeRB cell protein according to

$$R'_{U(IV),t_j} = \frac{\overline{C_{U(IV),t_{j+1}}} - \overline{C_{U(IV),t_j}}}{(t_{j+1} - t_j) \frac{(\overline{C_{FeRB,t_{j+1}}} + \overline{C_{FeRB,t_j}})}{2}}$$

where

$$\overline{C_{FeRB,t_j}} = \frac{\frac{1}{\alpha_{FeRB}} \sum_{i=1}^{N} X_{FeRB,t_j}}{\sum_{i=1}^{N} (1 - \phi_{i,t_j}) \rho_{sediment}} \quad (9)$$

Here $\overline{C_{FeRB,t_j}}$ is the averaged concentration of FeRB at time t_j (mg of FeRB/g sediment), X_{FeRB,t_j} is the cell density at time t_j (cells/cm^3 sediment). The conversion factor α_{FeRB} of 2.5×10^{12} cells/(g FeRB cell protein) was assumed to convert the cell numbers into cell proteins.[72] Therefore, R' is a rate normalized by the amount of cell protein and does not depend on microbial abundance.

RESULTS AND DISCUSSION

Breakthrough Curves. The modeling outputs and breakthrough data from six monitoring wells in the NBIZ and BIZ are compared in Figure 3. The other 11 monitoring wells are at similar levels of agreement between data and model output and are not shown for the sake of conciseness. The model reproduced the time when the pulses of injected constituents arrived. The data−model disagreement in some wells, for example, for acetate in well CD16, is likely due to the

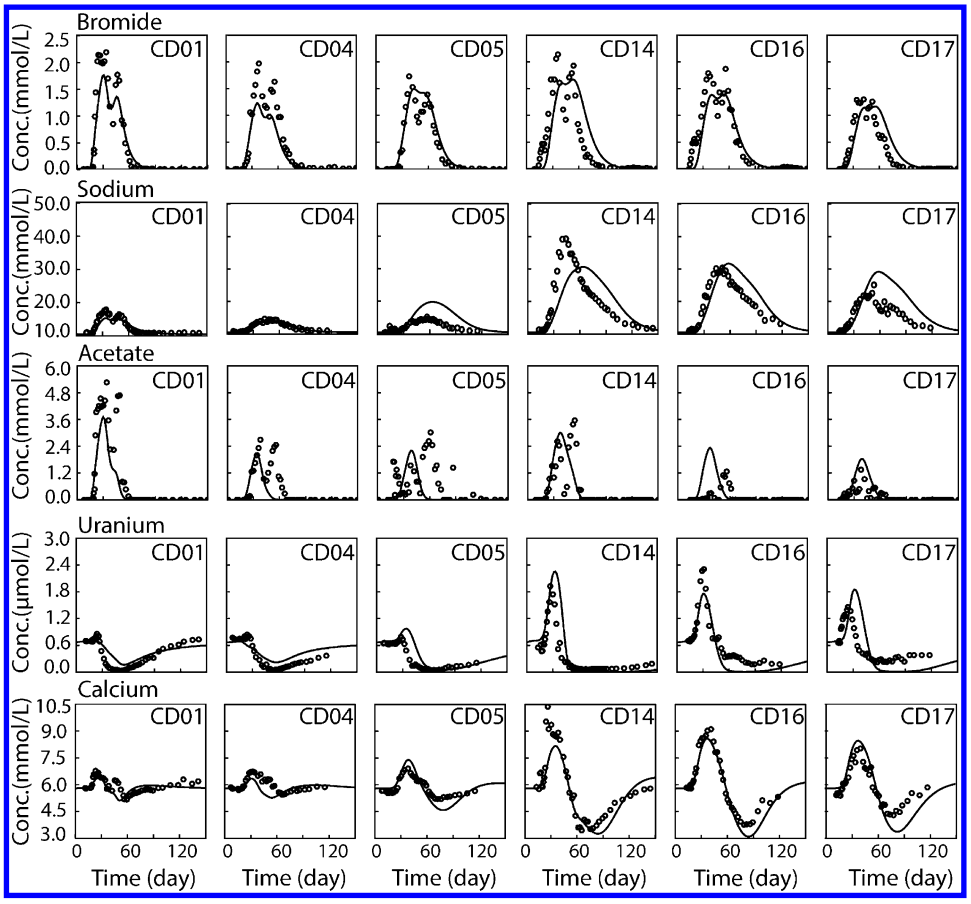

Figure 3. Comparisons of bromide, sodium, acetate, uranium, and calcium breakthrough data (circles) with the modeling output (lines) from three monitoring wells in the no-bicarbonate injection zone (CD01, CD04, and CD05 in NBIZ) and three wells in the bicarbonate injection zone (CD14, CD16, and CD17 in BIZ). Aqueous concentrations of sodium, uranium, and calcium were much higher in the BIZ wells than in the NBIZ wells due to the addition of sodium bicarbonate and the induced desorption and ion exchange reactions. The model captured the up and down of concentrations during and after the injection period.

uncertainty associated with the inferred spatial distribution of properties based on limited data points.

The good fit between data and modeling output for multiple species indicates that the model has captured the system dynamics, which constrained the estimation of aqueous species, mineral precipitates, and biomass. The model fit to the nonreactive bromide data confirmed the reasonable distribution of hydraulic conductivity. Given the fact that all injectates contained sodium, sodium concentrations increased significantly and reached as high as 0.041 mol/L. Acetate was injected at a concentration higher than that of bromide. However, its peak was much smaller due to its consumption by bacteria. The U(VI) concentration during bicarbonate injection increased much more in the BIZ than that in the NBIZ due to the desorption from the solid phases. The rapid decrease of U(VI) concentrations upon acetate injection indicates the occurrence of bioreduction. This was confirmed by comparing two simulation cases that included and excluded U(VI) bioreduction. Although not shown here, the case without U(VI) bioreduction showed negligible decrease in U(VI) concentration upon acetate injection. In addition, a large body of literature has confirmed the occurrence of U(VI) bioreduction products, including iron sulfides, biogenic $UO_2(s)$, and biomass-bound monomeric U(IV),[73] at the Rifle site. The techniques used include molecular-scale spectroscopic observations,[37,74] isotopic fractionation analysis,[75] and microbial analysis,[76] to name just a few. Calcium concentrations increased first due to the ion exchange with the injected sodium and decreased later due to calcite precipitation.

Although not shown here, sensitivity analysis indicated that the sodium breakthrough was largely determined by equilibrium constants of ion exchange reactions and that acetate breakthrough was controlled by the rates of iron and sulfate bioreduction. The increase of U(VI) during the bicarbonate injection stage was determined by the surface complexation, while the later decrease upon acetate injection was controlled by the U(VI) bioreduction kinetics, similar to the observations in the in situ U(VI) bioremediation experiments at the Oak Ridge site.[18] The early peak of calcium was governed by ion exchange, and the later decrease was controlled by calcite precipitation kinetics.

Spatial and Temporal Evolution at the Local Scale. The dynamic interactions between the biogeochemical reactions and transport are illustrated in Figure 4 using the injectate profiles at different experimental stages. The plume of total inorganic carbonate (TIC) was formed near the bicarbonate injection wells on day 12, 7 days after the injection started. Over time the plume expanded downstream with increasing concentration until day 27 upon the stop of the injection. After that the plume continued to expand; however this occurred with decreasing peak concentration due to its migration to a larger area and calcite precipitation. Although the

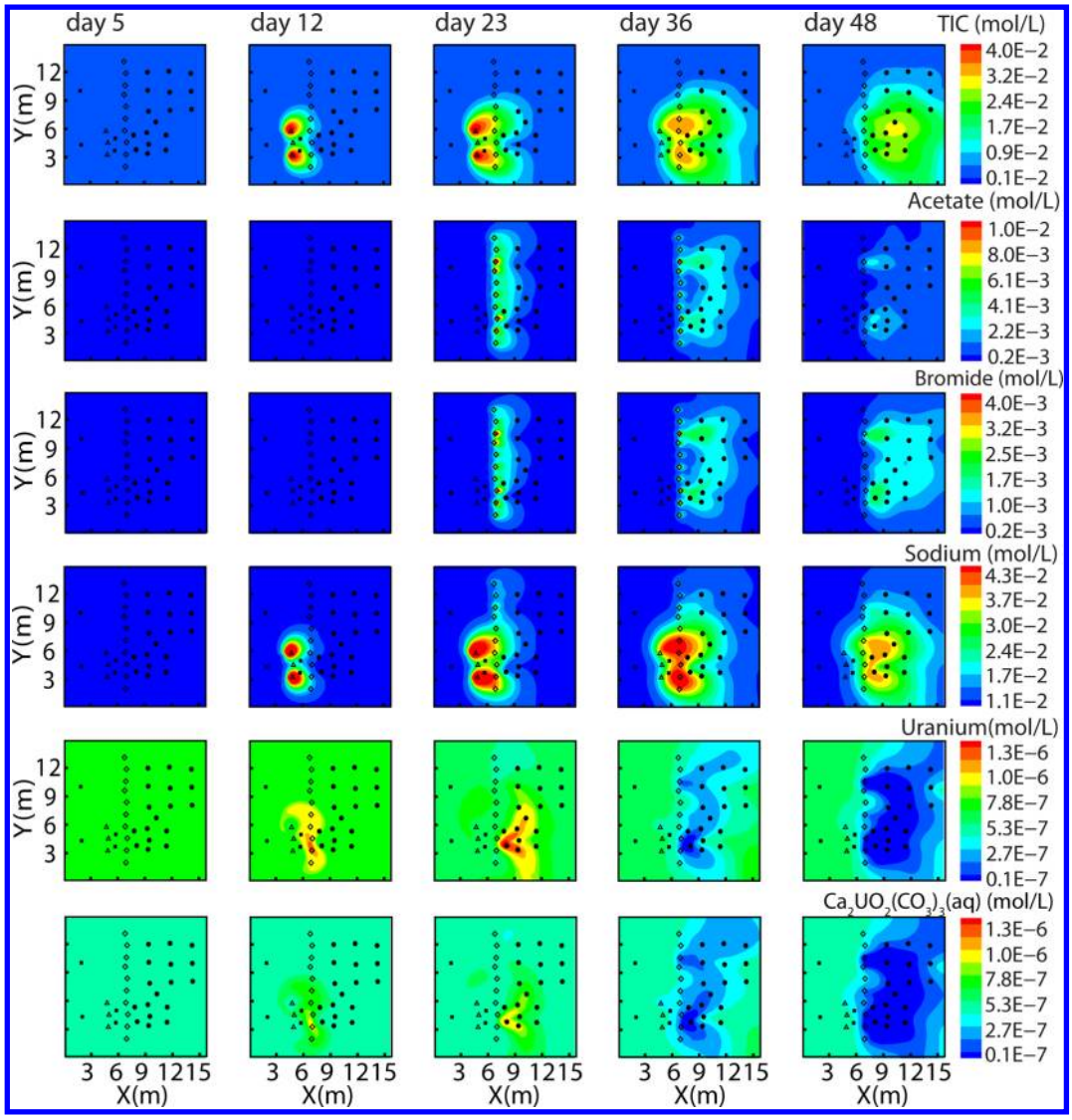

Figure 4. Predicted spatial and temporal evolution of all injectates and aqueous U(VI) species, including total inorganic carbon (TIC), acetate, bromide, sodium, total aqueous U(VI), and $Ca_2UO_2(CO_3)_3(aq)$. Sodium bicarbonate was injected starting on day 5, while sodium acetate and sodium bromide were injected starting on day 12. The difference between acetate and bromide indicates the amount of acetate consumption by microbe-mediated redox reactions. $Ca_2UO_2(CO_3)_3(aq)$ was the dominant aqueous U(VI) species, which typically occupied 60.5−80.0% of the total U(VI).

bioreduction reactions also generated bicarbonate, the concentration was so much lower than that of injected bicarbonate that this was not obvious from the profiles of NBIZ.

The injection of acetate and bromide started on day 12. To compare the dynamics of these two simultaneously injected species, the color scale was carefully chosen to reflect their mole ratio in the injected mixture. In this way, if acetate was as nonreactive as bromide, its plume should look very similar to the bromide plume. The difference in the two plumes was the result of the bioreduction reactions. On day 23, the two plumes were still similar, indicating a latency of the bioreduction limited by the slow biomass accumulation early on. At later times, while bromide migrated down gradient covering a large region, acetate was quickly consumed, leading to a much smaller plume with much lower concentrations. Because all injected reagents involved sodium, sodium profiles resembled the summation of bicarbonate and bromide profiles, except that some sodium was consumed by ion exchange. Bicarbonate injection heavily outpaced the injection of acetate and bromide such that the sodium plume was more similar to the TIC plume.

Figure 4 shows the profiles of total aqueous U(VI) and $Ca_2UO_2(CO_3)_3(aq)$ in the last two rows. The bicarbonate injection mobilized U(VI) from the sediment, which generated a U(VI) plume in the immediate down gradient of the bicarbonate wells on day 12. No such plume was formed in NBIZ. Over time this plume migrated to the down gradient regions. At later times, the acetate-stimulated FeRB bioreduced U(VI), resulting in a U(VI) depletion area direct down gradient of the acetate injection wells. Consistent with previously reported U(VI) speciation,[45,77,78] $Ca_2UO_2(CO_3)_3(aq)$ was dominant among the 23 U(VI)-containing species (Table S3, Supporting Information), occupying 60.5−80.0% of total U(VI). The $Ca_2UO_2(CO_3)_3(aq)$ plume was therefore similar to that of total U(VI).

Profiles of solid phases, FeRB, and bioreduction rates are shown in Figure 5. During acetate injection, the Fe(III) bioreduction rate increased considerably from day 12 to 36.

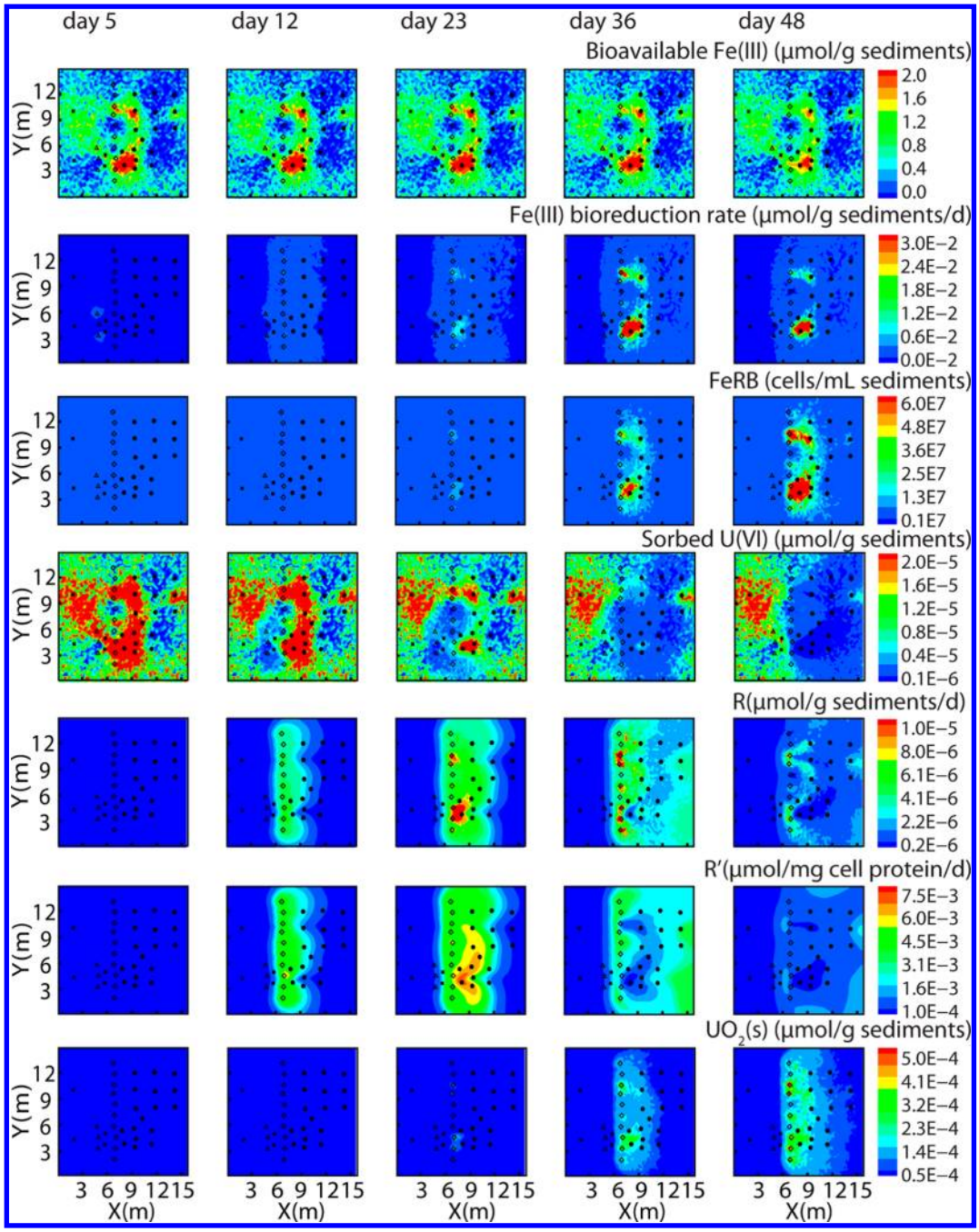

Figure 5. Predicted spatial and temporal profiles of bioavailable Fe(III), Fe(III) bioreduction rates, FeRB, adsorbed U(VI), U(VI) bioreduction rates (R and R′), and reduced U(IV) in the form of UO_2(s). The bioreduction rates and the FeRB are characterized by a few "hot spots" immediately down gradient of the injection wells, where the rates and biomass concentrations were orders of magnitude higher than those in the rest of the domain.

The profiles of Fe(III) bioreduction rates highlights a few hot spots with 1−2 orders higher rates in comparison to those in the rest of the domain. The hot spots were close to the injection wells, where acetate concentrations were high, which triggered abundant FeRB growth. Although FeRB continued to grow, the reduction rates decreased on day 48 after the acetate injection stopped. Comparison of the initial Fe(III) concentration in the BIZ and NBIZ shows that the Fe(III) originally in the BIZ was 36.5% higher than that in the NBIZ, leading to higher Fe(III) bioreduction rate and more FeRB in general.

Before the bicarbonate injection, adsorbed U(VI) positively correlated to bioavailable Fe(III), with U(VI) mainly adsorbed onto clay and iron oxide surfaces having larger surface area and lower permeability. On day 12, sorbed U(VI) concentration decreased in regions close to the bicarbonate injection wells, indicating the desorption and migration of U(VI). This corroborated the U(VI) increase in Figures 3 and 4. This depletion zone continued to expand due to desorption and later bioreduction. Interestingly, although desorption occurred earlier in the BIZ, desorption also occurred in the NBIZ at later times, as indicated by the disappearance of the red zone in the NBIZ. This U(VI) desorption was induced by bioreduction, which lowered aqueous U(VI) concentrations.

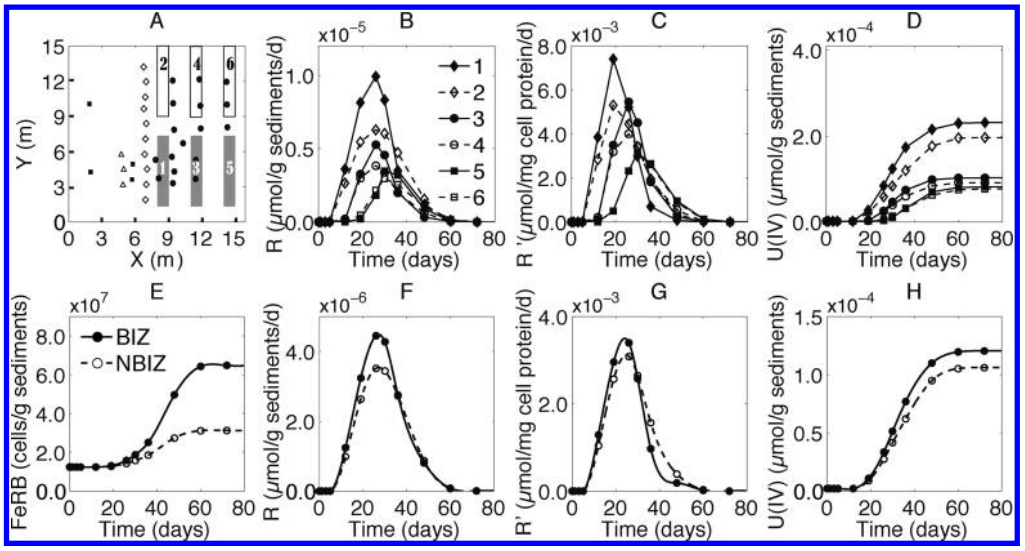

Figure 6. Evolution of bioreduction rates in six different observation zones and the entire domain. (A) Location of the three pairs of observation windows with different distances to the injection wells. (B) Temporal evolution of the average bioreduction rates in each observation zone (R, in μmol/g sediments/d). (C) Evolution of the average bioreduction rates in each observation zone normalized by the amount of cell protein (R', in μmol/mg cell protein/d). (D) Cumulative U(IV) concentration in each zone (μmol/g sediments). Temporal evolution in BIZ and NBIZ for (E) FeRB (cells/g sediments), (F) U bioreduction rates (R, in μmol/g sediments/d), (G) U bioreduction rates for BIZ and NBIZ (R', in μmol/mg of cell protein/d), and (H) cumulative bioreduced U(IV) concentration for BIZ and NBIZ (μmol/g sediments).

Similar to that of Fe(III) bioreduction rates, the profiles of U(VI) bioreduction rates and the precipitated UO_2(s) highlight the hot spots close to the acetate injection wells where electron donor, acceptor, and bacteria concentrations were at their maxima. Although the front of the injected plume migrated across the domain (Figure 4), the location of the hot spots remained fixed, emphasizing the importance of coexistence of all participating components. The U(IV) accumulation rates were higher in the BIZ than those in the NBIZ on days 23 and 36. This difference decreased temporally, as observed by similar bioreduction and U(IV) accumulation rates at later times. Interestingly, the temporal evolution of the biomass-normalized rates R' (μmol/mg cell protein/d) was different from that of R in μmol/g sediments/d. The normalized R' was in general higher on day 23 than on day 36, largely because the concentrations of uranium were higher (Figure 4) on day 23. On day 36, U(VI) concentrations were much lower due to consumption by more abundant FeRB at later time.

Evolution of Uranium Bioreduction at the Intermediate and Field Scales. To understand the effects of bicarbonate injection on U(VI) bioreduction rates, we chose three pairs of observation zones with the same total area of 6 m^2. They are located at 1.25 m down gradient of the injection wells (1, 2), 4.25 m down gradient (3, 4), and 7.25 m down gradient (5, 6), as shown in Figure 6A. For each pair, one is in the BIZ and the other is in the NBIZ. As can be observed from Figure 6B,C, the average bioreduction rates are generally higher and reach their maxima earlier close to the injection wells (zones 1 and 2) in comparison to those in other zones because acetate arrived earlier at higher concentrations (Figure 4). In locations more down gradient, the acetate arrived later at lower concentration, leading to varying location of the "hot moments". Within each pair, the rates R (in (μmol of reduced U(VI))/g sediment/d) in the BIZ were consistently larger than those in the NBIZ, with the largest difference being 57.9% on day 23 close to the injection wells. With the different biomass abundances in the two zones, the rates normalized by the biomass (in units of mg of cell protein), R', in the two zones differed by a maximum of 39.4% (Figure 6C). This indicates that the bicarbonate injection temporally enhanced the U(VI) desorption early on. Its long-term effects on U(VI) bioreduction, however, were almost negligible, likely owing to the finite supply of sorbed U(VI) extractable through bicarbonate addition. Figure 6D shows the faster and larger amount of U(IV) accumulation close to the injection wells in comparison to other locations, emphasizing the importance of hot spots in determining larger scale rates.

At the field scale, the effect of bicarbonate injection became even less pronounced. While close to the injection wells the bicarbonate injection led to a maximum of 39.4% difference in bioreduction rate R' on day 23, this effect was attenuated into a maximum of 10.0% at the field scale on the same day. Figure 6E shows that the biomass in the BIZ almost doubled that of the NBIZ at the end of experiment. However, field scale U(IV) precipitation rates in units of μmol/g sediment/day and in units of μmol/mg cell protein/day were only slightly higher in the BIZ than in the NBIZ (Figure 6F,G), presumably because U(VI) bioreduction was not limited by the amount of available FeRB. Instead, it was limited by the available U(VI) at the micromolar level. The bicarbonate injection temporarily "washed out" the desorbed U(VI) from the solid phase. However, in the long term, it was the up gradient background groundwater that continuously provided aqueous U(VI), which was similar for both the BIZ and NBIZ. Our calculations show that the total desorbed U(VI) was only 21.3% of the total amount of reduced U(VI), indicating a relatively minor impact on U(VI) bioreduction at the field scale. The similarity between the field scale and the intermediate scale curves of the observation zones 1 and 2 emphasizes the dominance of rates close to the injection wells.

Uranium Bioreduction Rates across Scales. Uranium bioreduction has been extensively studied using batch reactors and columns with pure cultures and natural microbial samples. To a much lesser extent, bioreduction rates have also been

examined in field experiments (individual wells).[17,18,22] To put the rates from this work in the context of others, we define several length scales. For the rates from well-mixed batch reactors, the length scale is the radius of cells on the order of 10^{-6} m. In contrast, if the bioreduction rates are calculated by averaging over a certain area, the length scale is the scale of the observation window. Here the local scale is in tens of centimeters and the field scale is in tens of meters. Figure 7

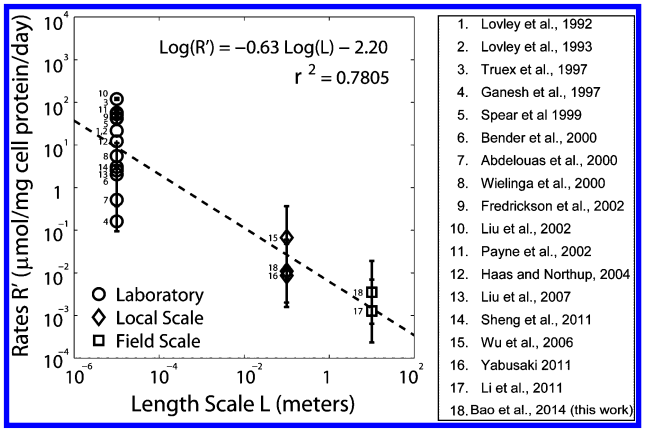

Figure 7. Compiled uranium(VI) bioreduction rates in units of μmol/mg cell protein/d. The dashed line shows the log−log rate dependence on the measurement length scale. The error bars are based on the range of the FeRB cell density from 3×10^5 to 9×10^6 cells/mL of the sediment in natural environments.[23]

summarizes the calculated "maximum" bioreduction rates during the active bioreduction period on the basis of literature data (calculation details in Table S7, Supporting Information).

As shown in Figure 7, the batch reactor rates are 1−5 orders of magnitude higher than those at the local and field scales. The rates obtained in this work are in good agreement with previously reported values.[27,39] This is because rates of pure cultures at the batch reactor scale often reflect the bioreduction potentials of certain bacterium at full functioning. In subsurface environments, however, different electron donors selectively stimulate bacteria species with different kinetics[17,18,76] and the rates often reflect the average bioreduction capability of bacterial communities. In addition, at the field scale, the biogeochemical conditions, including the concentrations of electron donors and acceptors, are typically dictated by the heterogeneous spatial distribution of flow and transport properties that determine the extent of mixing, as has been extensively reported.[79−81] These biogeochemical environments are substantially different from laboratory conditions, often leading to orders of magnitude lower microbial activity and rates.[23,82] The scaling effects, however, are not merely a result of spatial heterogeneity. Even in homogeneous systems, rates decrease due to the decreasing level of mixing with increasing length scale. This trend of decreasing rates with increasing length scale has been similarly observed for chemical weathering rates and has been extensively discussed in the geochemical community.[83,84] Navarre-Sitchler and Brantley proposed to use the resolution of measurement to quantify the scale dependency of basalt weathering and obtained a similar dependence of rates on spatial scales.[85] The log R' versus log L relationship in Figure 7 provides an orders-of-magnitude estimation of uranium bioreduction rates at different scales.

Environmental Implications. This work assessed the scale-dependent evolution of uranium bioreduction rates in the heterogeneous subsurface during a field biostimulation experiment in 2010. The results show that acetate injection perturbed the subsurface and generated hot spots characterized by orders of magnitude higher rates in comparison to those in the rest of the domain. These hot spots typically occur close to the injection wells, where all reacting components exist at maximum concentrations. The arrival times of the hot moments for particular locations increase with increasing distances from the injection wells due to the requisite travel time. The characteristics of the hot moments and hot spots, however, depend largely on the reactive nature of the biogeochemical systems. For example, the occurrence of the close-to-well hot spots, to a certain extent, is largely due to the fast-degrading nature of acetate as an electron donor; a slow-degrading donor may lead to hot spots much more distal from the injection wells, as has been observed for the injection of emulsified vegetable oil in an U(VI)-contaminated aquifer.[17,25] At Rifle, the Fe(III) minerals contain both Fe oxides and those associated with clay. If the Fe(III) minerals are less available with lower reactivity, the hot spots are also likely to occur much farther away from the injection wells.

The results show that the bicarbonate injection did enhance local U(VI) bioreduction rates temporarily and locally, consistent with other observations.[86] However, its effect at the field scale and over longer time scales is relatively small (a maximum of 10.0%). The U(VI) desorption through bicarbonate injection represents an increase of only 21.3% of the total reduced U(VI) over the total biostimulation period of 38 days, with local rates in hot spots dominating rates at the field scale. As a result, even though some local rates may be similar to those measured in well-mixed batch reactors, field scale rates are much smaller, given volumetric averaging over a much larger domain.

■ ASSOCIATED CONTENT

Ⓢ Supporting Information

Text and tables giving details of the information given in Materials and Methods, including information on the Rifle site, reaction network, and thermodynamics. This material is available free of charge via the Internet at http://pubs.acs.org.

■ AUTHOR INFORMATION

Corresponding Author

*E-mail for L.L.: lili@eme.psu.edu.

Notes

The authors declare no competing financial interest.

■ ACKNOWLEDGMENTS

Funding was provided by the U.S. Department of Energy, Office of Sciences, Biological and Environmental Research to the LBNL Sustainable Systems Scientific Focus Area under Award Number DE-AC02-05CH1123 and through a subcontract to Penn State University. We acknowledge the Rifle IFRC research team for facilitating collaboration and access to Rifle data. We acknowledge the associate editor Dr. Jorge Gardea-Torresdey for handling this paper and two anonymous reviewers for their diligent and constructive reviews that have significantly improved the paper.

REFERENCES

(1) Begg, J. D. C.; Burke, I. T.; Lloyd, J. R.; Boothman, C.; Shaw, S.; Charnock, J. M.; Morris, K. Bioreduction behavior of U(VI) sorbed to sediments. *Geomicrobiol. J.* **2011**, *28* (2), 160−171.

(2) Grenthe, I.; Stumm, W.; Laaksuharju, M.; Nilsson, A.; Wikberg, P. Redox potentials and redox reactions in deep groundwater systems. *Chem. Geol.* **1992**, *98* (1), 131−150.

(3) Lovley, D. R.; Roden, E. E.; Phillips, E.; Woodward, J. Enzymatic iron and uranium reduction by sulfate-reducing bacteria. *Mar. Geol.* **1993**, *113* (1), 41−53.

(4) Wielinga, B.; Bostick, B.; Hansel, C. M.; Rosenzweig, R. F.; Fendorf, S. Inhibition of bacterially promoted uranium reduction: Ferric (hydr) oxides as competitive electron acceptors. *Environ. Sci. Technol.* **2000**, *34* (11), 2190−2195.

(5) Brooks, S. C.; Fredrickson, J. K.; Carroll, S. L.; Kennedy, D. W.; Zachara, J. M.; Plymale, A. E.; Kelly, S. D.; Kemner, K. M.; Fendorf, S. Inhibition of bacterial U(VI) reduction by calcium. *Environ. Sci. Technol.* **2003**, *37* (9), 1850−1858.

(6) Ganesh, R.; Robinson, K. G.; Reed, G. D.; Sayler, G. S. Reduction of hexavalent uranium from organic complexes by sulfate-and iron-reducing bacteria. *Appl. Environ. Microbiol.* **1997**, *63* (11), 4385−4391.

(7) Sheng, L.; Szymanowski, J.; Fein, J. B. The effects of uranium speciation on the rate of U (VI) reduction by *Shewanella oneidensis* MR-1. *Geochim. Cosmochim. Acta* **2011**, *75* (12), 3558−3567.

(8) Payne, R. B.; Gentry, D. M.; Rapp-Giles, B. J.; Casalot, L.; Wall, J. D. Uranium reduction by Desulfovibrio desulfuricans strain G20 and a cytochrome c3 mutant. *Appl. Environ. Microbiol.* **2002**, *68* (6), 3129−3132.

(9) Abdelouas, A.; Lutze, W.; Gong, W.; Nuttall, E. H.; Strietelmeier, B. A.; Travis, B. J. Biological reduction of uranium in groundwater and subsurface soil. *Sci. Total Environ.* **2000**, *250* (1), 21−35.

(10) Fredrickson, J. K.; Zachara, J. M.; Kennedy, D. W.; Liu, C.; Duff, M. C.; Hunter, D. B.; Dohnalkova, A. Influence of Mn oxides on the reduction of uranium(VI) by the metal-reducing bacterium *Shewanella putrefaciens*. *Geochim. Cosmochim. Acta* **2002**, *66* (18), 3247−3262.

(11) Truex, M. J.; Peyton, B. M.; Valentine, N. B.; Gorby, Y. A. Kinetics of U(VI) reduction by a dissimilatory Fe (III)-reducing bacterium under non-growth conditions. *Biotechnol. Bioeng.* **2000**, *55* (3), 490−496.

(12) Liu, C.; Gorby, Y. A.; Zachara, J. M.; Fredrickson, J. K.; Brown, C. F. Reduction kinetics of Fe(III), Co (III), U (VI), Cr(VI), and Tc(VII) in cultures of dissimilatory metal-reducing bacteria. *Biotechnol. Bioeng.* **2002**, *80* (6), 637−649.

(13) Wazne, M.; Korfiatis, G. P.; Meng, X. Carbonate effects on hexavalent uranium adsorption by iron oxyhydroxide. *Environ. Sci. Technol.* **2003**, *37* (16), 3619−3624.

(14) Waite, T.; Davis, J.; Payne, T.; Waychunas, G.; Xu, N. Uranium(VI) adsorption to ferrihydrite: Application of a surface complexation model. *Geochim. Cosmochim. Acta* **1994**, *58* (24), 5465−5478.

(15) Li, L.; Peters, C. A.; Celia, M. A. Upscaling geochemical reaction rates using pore-scale network modeling. *Adv. Water Resour.* **2006**, *29* (9), 1351−1370.

(16) Istok, J.; Senko, J.; Krumholz, L. R.; Watson, D.; Bogle, M. A.; Peacock, A.; Chang, Y.-J.; White, D. C. In situ bioreduction of technetium and uranium in a nitrate-contaminated aquifer. *Environ. Sci. Technol.* **2004**, *38* (2), 468−475.

(17) Watson, D. B.; Wu, W.; Mehlhorn, T.; Tang, G.; Earles, J.; Lowe, K.; Gihring, T. M.; Zhang, G.; Phillips, J.; Boyanov, M.; Spalding, B. P.; Schadt, C.; Kemner, K. M.; Criddle, C. S.; Jardine, P. M.; Brooks, S. C. In situ bioremediation of uranium with emulsified vegetable oil as the electron donor. *Environ. Sci. Technol.* **2013**, *47*, 6440−6448.

(18) Wu, W.-M.; Carley, J.; Gentry, T.; Ginder-Vogel, M. A.; Fienen, M.; Mehlhorn, T.; Yan, H.; Caroll, S.; Pace, M. N.; Nyman, J. Pilot-scale in situ bioremedation of uranium in a highly contaminated aquifer. 2. Reduction of U(VI) and geochemical control of U(VI) bioavailability. *Environ. Sci. Technol.* **2006**, *40* (12), 3986−3995.

(19) Scheibe, T. D.; Fang, Y.; Murray, C. J.; Roden, E. E.; Chen, J.; Chien, Y.-J.; Brooks, S. C.; Hubbard, S. S. Transport and biogeochemical reaction of metals in a physically and chemically heterogeneous aquifer. *Geosphere* **2006**, *2* (4), 220−235.

(20) Scheibe, T. D.; Hubbard, S. S.; Onstott, T. C.; DeFlaun, M. F. Lessons Learned from Bacterial Transport Research at the South Oyster Site. *Ground Water* **2011**, *49* (5), 745−763.

(21) Yabusaki, S. B.; Fang, Y.; Long, P. E.; Resch, C. T.; Peacock, A. D.; Komlos, J.; Jaffe, P. R.; Morrison, S. J.; Dayvault, R. D.; White, D. C.; Anderson, R. T. Uranium removal from groundwater via in situ biostimulation: Field-scale modeling of transport and biological processes. *J. Contam. Hydrol.* **2007**, *93* (1−4), 216−235.

(22) Yabusaki, S. B.; Fang, Y.; Williams, K. H.; Murray, C. J.; Ward, A. L.; Dayvault, R. D.; Waichler, S. R.; Newcomer, D. R.; Spane, F. A.; Long, P. E. Variably saturated flow and multicomponent biogeochemical reactive transport modeling of a uranium bioremediation field experiment. *J. Contam. Hydrol.* **2011**, *126* (3−4), 271−290.

(23) Li, L.; Gawande, N.; Kowalsky, M. B.; Steefel, C. I.; Hubbard, S. S. Physicochemical heterogeneity controls on uranium bioreduction rates at the field scale. *Environ. Sci. Technol.* **2011**, *45* (23), 9959−66.

(24) Li, L.; Steefel, C. I.; Kowalsky, M. B.; Englert, A.; Hubbard, S. S. Effects of physical and geochemical heterogeneities on mineral transformation and biomass accumulation during biostimulation experiments at Rifle, Colorado. *J. Contam. Hydrol.* **2010**, *112* (1−4), 45−63.

(25) Tang, G.; Watson, D. B.; Wu, W.-M.; Schadt, C. W.; Parker, J. C.; Brooks, S. C. U(VI) Bioreduction with Emulsified Vegetable Oil as the Electron Donor − Model Application to a Field Test. *Environ. Sci. Technol.* **2013**, *47* (7), 3218−3225.

(26) Luo, J.; Weber, F. A.; Cirpka, O. A.; Wu, W. M.; Nyman, J. L.; Carley, J.; Jardine, P. M.; Criddle, C. S.; Kitanidis, P. K. Modeling in-situ uranium(VI) bioreduction by sulfate-reducing bacteria. *J. Contam. Hydrol.* **2007**, *92* (1), 129−148.

(27) Spear, J. R.; Figueroa, L. A.; Honeyman, B. D. Modeling reduction of uranium U(VI) under variable sulfate concentrations by sulfate-reducing bacteria. *Appl. Environ. Microbiol.* **2000**, *66* (9), 3711−3721.

(28) Davis, J. A.; Yabusaki, S. B.; Steefel, C. I.; Zachara, J. M.; Curtis, G. P.; Redden, G. D.; Criscenti, L. J.; Honeyman, B. D. Assessing conceptual models for subsurface reactive transport of inorganic contaminants. *EOS, Trans. Am. Geophys. Union* **2004**, *85* (44), 449−455.

(29) Liu, C. X.; Shang, J. Y.; Kerisit, S.; Zachara, J. M.; Zhu, W. H. Scale-dependent rates of uranyl surface complexation reaction in sediments. *Geochim. Cosmochim. Acta* **2013**, *105*, 326−341.

(30) Liu, C.; Shi, Z.; Zachara, J. M. Kinetics of Uranium(VI) Desorption from Contaminated Sediments: Effect of Geochemical Conditions and Model Evaluation. *Environ. Sci. Technol.* **2009**, *43* (17), 6560−6566.

(31) Qafoku, N. P.; Zachara, J. M.; Liu, C. X.; Gassman, P. L.; Qafoku, O. S.; Smith, S. C. Kinetic desorption and sorption of U(VI) during reactive transport in a contaminated Hanford sediment. *Environ. Sci. Technol.* **2005**, *39* (9), 3157−3165.

(32) Fox, P. M.; Davis, J. A.; Hay, M. B.; Conrad, M. E.; Campbell, K. M.; Williams, K. H.; Long, P. E., Rate-limited U(VI) desorption during a small-scale tracer test in a heterogeneous uranium-contaminated aquifer. *Water Resour. Res.* **2012**, *48*.

(33) Phillips, E. J. P.; Landa, E. R.; Lovley, D. R. Remediation of Uranium Contaminated Soils with Bicarbonate Extraction and Microbial U(Vi) Reduction. *J. Ind. Microbiol.* **1995**, *14* (3−4), 203−207.

(34) Anderson, R. T.; Vrionis, H. A.; Ortiz-Bernad, I.; Resch, C. T.; Long, P. E.; Dayvault, R.; Karp, K.; Marutzky, S.; Metzler, D. R.; Peacock, A.; White, D. C.; Lowe, M.; Lovley, D. R. Stimulating the in situ activity of Geobacter species to remove uranium from the groundwater of a uranium-contaminated aquifer. *Appl. Environ. Microbiol.* **2003**, *69* (10), 5884−5891.

(35) Vrionis, H. A.; Anderson, R. T.; Ortiz-Bernad, I.; O'Neill, K. R.; Resch, C. T.; Peacock, A. D.; Dayvault, R.; White, D. C.; Long, P. E.;

Lovley, D. R. Microbiological and geochemical heterogeneity in an in situ uranium bioremediation field site. *Appl. Environ. Microbiol.* **2005**, *71* (10), 6308−6318.
(36) Li, L.; Steefel, C. I.; Williams, K. H.; Wilkins, M. J.; Hubbard, S. S. Mineral Transformation and Biomass Accumulation Associated With Uranium Bioremediation at Rifle, Colorado. *Environ. Sci. Technol.* **2009**, *43* (14), 5429−5435.
(37) Bargar, J. R.; Williams, K. H.; Campbell, K. M.; Long, P. E.; Stubbs, J. E.; Suvorova, E. I.; Lezama-Pacheco, J. S.; Alessi, D. S.; Stylo, M.; Webb, S. M.; Davis, J. A.; Giammar, D. E.; Blue, L. Y.; Bernier-Latmani, R. Uranium redox transition pathways in acetate-amended sediments. *Proc. Natl. Acad. Sci. U.S.A.* **2013**, *110* (12), 4506−4511.
(38) Williams, K. H.; Long, P. E.; Davis, J. A.; Wilkins, M. J.; N'Guessan, A. L.; Steefel, C. I.; Yang, L.; Newcomer, D.; Spane, F. A.; Kerkhof, L. J.; McGuinness, L.; Dayvault, R.; Lovley, D. R. Acetate Availability and its Influence on Sustainable Bioremediation of Uranium-Contaminated Groundwater. *Geomicrobiol. J.* **2011**, *28* (5−6), 21.
(39) Campbell, K. M.; Kukkadapu, R. K.; Qafoku, N. P.; Peacock, A. D.; Lesher, E.; Williams, K. H.; Bargar, J. R.; Wilkins, M. J.; Figueroa, L.; Ranville, J.; Davis, J. A.; Long, P. E. Geochemical, mineralogical and microbiological characteristics of sediment from a naturally reduced zone in a uranium-contaminated aquifer. *Appl. Geochem.* **2012**, *27* (8), 1499−1511.
(40) Shiel, A. E.; Laubach, P. G.; Johnson, T. M.; Lundstrom, C. C.; Long, P. E.; Williams, K. H. No Measurable Changes in U-238/U-235 due to Desorption-Adsorption of U(VI) from Groundwater at the Rifle, Colorado, Integrated Field Research Challenge Site. *Environ. Sci. Technol.* **2013**, *47* (6), 2535−2541.
(41) Butler, J. J., Jr. *The design, performance, and analysis of slug tests*; Lewis Publishers, CRC Press: Boca Raton, FL, 1998.
(42) Webster, R.; Oliver, M. A. *Geostatistics for environmental scientists*, 2nd ed.; Wiley: Chichester, U.K., 2007.
(43) Eggleston, J.; Rojstaczer, S. Identification of large-scale hydraulic conductivity trends and the influence of trends on contaminant transport. *Water Resour. Res.* **1998**, *34* (9), 2155−2168.
(44) Knotters, M.; Brus, D. J.; Voshaar, J. H. O. A Comparison of Kriging, Co-Kriging and Kriging Combined with Regression for Spatial Interpolation of Horizon Depth with Censored Observations. *Geoderma* **1995**, *67* (3−4), 227−246.
(45) Williams, K. H.; Long, P. E.; Davis, J. A.; Wilkins, M. J.; N'Guessan, A. L.; Steefel, C. I.; Yang, L.; Newcomer, D.; Spane, F. A.; Kerkhof, L. J.; McGuinness, L.; Dayvault, R.; Lovley, D. R. Acetate Availability and its Influence on Sustainable Bioremediation of Uranium-Contaminated Groundwater. *Geomicrobiol. J.* **2011**, *28* (5−6), 519−539.
(46) Singha, K.; Li, L.; Day-Lewis, F. D.; Regberg, A. B. Quantifying solute transport processes: Are chemically "conservative" tracers electrically conservative? *Geophysics* **2011**, *76* (1), F53−F63.
(47) Brunet, J. L.; Li, L.; Karpyn, Z. T.; Kutchko, B.; Strazisar, B.; Bromhal, G. Dynamic evolution of compositional and transport properties under conditions relevant to geological carbon sequestration. *Energy Fuels* **2013**, *27* (8), 4208−4220.
(48) Molins, S.; Trebotich, D.; Steefel, C. I.; Shen, C., An investigation of the effect of pore scale flow on average geochemical reaction rates using direct numerical simulation. *Water Resour. Res.* **2012**, *48*.
(49) Lichtner, P. C. Continuum Model for Simultaneous Chemical-Reactions and Mass-Transport in Hydrothermal Systems. *Geochim. Cosmochim. Acta* **1985**, *49* (3), 779−800.
(50) Steefel, C. I.; Lasaga, A. C. A Coupled Model for Transport of Multiple Chemical-Species and Kinetic Precipitation Dissolution Reactions with Application to Reactive Flow in Single-Phase Hydrothermal Systems. *Am. J. Sci.* **1994**, *294* (5), 529−592.
(51) Rittmann, B. E.; McCarty, P. L. *Environmental biotechnology*; McGraw-Hill: New York, 2001.
(52) Rutgers, M.; van der Gulden, H. M.; Dam, K. Thermodynamic efficiency of bacterial growth calculated from growth yield of *Pseudomonas oxalaticus* OX1 in the chemostat. *Biochim. Biophys. Acta, Bioenerg.* **1989**, *973* (2), 302−307.
(53) Cord-Ruwisch, R.; Lovley, D. R.; Schink, B. Growth of Geobacter sulfurreducens with acetate in syntrophic cooperation with hydrogen-oxidizing anaerobic partners. *Appl. Environ. Microbiol.* **1998**, *64* (6), 2232−2236.
(54) Esteve-Núñez, A.; Rothermich, M.; Sharma, M.; Lovley, D. Growth of Geobacter sulfurreducens under nutrient-limiting conditions in continuous culture. *Environ. Microbiol.* **2005**, *7* (5), 641−648.
(55) Mahadevan, R.; Bond, D.; Butler, J.; Esteve-Nunez, A.; Coppi, M.; Palsson, B.; Schilling, C.; Lovley, D. Characterization of metabolism in the Fe(III)-reducing organism Geobacter sulfurreducens by constraint-based modeling. *Appl. Environ. Microbiol.* **2006**, *72* (2), 1558−1568.
(56) VanBriesen, J. Evaluation of methods to predict bacterial yield using thermodynamics. *Biodegradation* **2002**, *13*, 171−190.
(57) Liu, C.; Zachara, J. M.; Fredrickson, J. K.; Kennedy, D. W.; Dohnalkova, A. Modeling the inhibition of the bacterial reduction of U (VI) by β-MnO2 (s). *Environ. Sci. Technol.* **2002**, *36* (7), 1452−1459.
(58) Monod, J. The Growth of Bacterial Cultures. *Annu. Rev. Microbiol.* **1949**, *3*, 371−394.
(59) Rittmann, B. E.; McCarty, P. L. *Environmental biotechnology: principles and applications*; McGraw-Hill: Boston, 2001.
(60) LaRowe, D. E.; Dale, A. W.; Amend, J. P.; Van Cappellen, P. Thermodynamic limitations on microbially catalyzed reaction rates. *Geochim. Cosmochim. Acta* **2012**, *90*, 96−109.
(61) Jin, Q.; Bethke, C. M. The thermodynamics and kinetics of microbial metabolism. *Am. J. Sci.* **2007**, *307* (4), 643−677.
(62) Jin, Q. S.; Bethke, C. M. Predicting the rate of microbial respiration in geochemical environments. *Geochim. Cosmochim. Acta* **2005**, *69* (5), 1133−1143.
(63) Wielinga, B.; Bostick, B.; Hansel, C. M.; Rosenzweig, R. F.; Fendorf, S. Inhibition of Bacterially Promoted Uranium Reduction: Ferric (Hydr)oxides as Competitive Electron Acceptors. *Environ. Sci. Technol.* **2000**, *34* (11), 2190−2195.
(64) Liger, E.; Charlet, L.; Van Cappellen, P. Surface catalysis of uranium (VI) reduction by iron(II). *Geochim. Cosmochim. Acta* **1999**, *63* (19), 2939−2955.
(65) Jeon, B. H.; Dempsey, B. A.; Burgos, W. D.; Barnett, M. O.; Roden, E. E. Chemical reduction of U(VI) by Fe(II) at the solid-water interface using natural and synthetic Fe(III) oxides. *Environ. Sci. Technol.* **2005**, *39* (15), 5642−5649.
(66) Roden, E. E.; Zachara, J. M. Microbial reduction of crystalline iron(III) oxides: Influence of oxide surface area and potential for cell growth. *Environ. Sci. Technol.* **1996**, *30* (5), 1618−1628.
(67) Lovley, D. R.; Phillips, E. J. P.; Gorby, Y. A.; Landa, E. R. Microbial reduction of uranium. *Nature* **1991**, *350* (6317), 413−416.
(68) Senko, J. M.; Istok, J. D.; Suflita, J. M.; Krumholz, L. R. In-situ evidence for uranium immobilization and remobilization. *Environ. Sci. Technol.* **2002**, *36* (7), 1491−1496.
(69) Williams, K. H.; Kemna, A.; Wilkins, M. J.; Druhan, J.; Arntzen, E.; N'Guessan, A. L.; Long, P. E.; Hubbard, S. S.; Banfield, J. F. Geophysical Monitoring of Coupled Microbial and Geochemical Processes During Stimulated Subsurface Bioremediation. *Environ. Sci. Technol.* **2009**, *43* (17), 6717−6723.
(70) Griebler, C.; Mindl, B.; Slezak, D.; Geiger-Kaiser, M. Distribution patterns of attached and suspended bacteria in pristine and contaminated shallow aquifers studied with an in situ sediment exposure microcosm. *Aquat. Microb. Ecol.* **2002**, *28* (2), 117−129.
(71) Lloyd, J. R. Microbial reduction of metals and radionuclides. *FEMS Microbiol. Rev.* **2003**, *27* (2−3), 411−425.
(72) Roden, E. E.; Urrutia, M. M. Ferrous iron removal promotes microbial reduction of crystalline iron(III) oxides. *Environ. Sci. Technol.* **1999**, *33* (11), 1847−1853.
(73) Qafoku, N. P.; Gartman, B. N.; Kukkadapu, R. K.; Arey, B. W.; Williams, K. H.; Mouser, P. J.; Heald, S. M.; Bargar, J. R.; Janot, N.; Yabusaki, S.; Long, P. E. Geochemical and mineralogical investigation

of uranium in multi-element contaminated, organic-rich subsurface sediment. *Appl. Geochem.* **2014**, *42* (0), 77−85.
(74) Stoliker, D. L.; Campbell, K. M.; Fox, P. M.; Singer, D. M.; Kaviani, N.; Carey, M.; Peck, N. E.; Bargar, J. R.; Kent, D. B.; Davis, J. A. Evaluating Chemical Extraction Techniques for the Determination of Uranium Oxidation State in Reduced Aquifer Sediments. *Environ. Sci. Technol.* **2013**, *47* (16), 9225−9232.
(75) Bopp, C. J.; Lundstrom, C. C.; Johnson, T. M.; Sanford, R. A.; Long, P. E.; Williams, K. H. Uranium 238U/235U Isotope Ratios as Indicators of Reduction: Results from an in situ Biostimulation Experiment at Rifle, Colorado, U.S.A. *Environ. Sci. Technol.* **2010**, *44* (15), 5927−5933.
(76) Anderson, R. T.; Vrionis, H. A.; Ortiz-Bernad, I.; Resch, C. T.; Long, P. E.; Dayvault, R.; Karp, K.; Marutzky, S.; Metzler, D. R.; Peacock, A. Stimulating the in situ activity of Geobacter species to remove uranium from the groundwater of a uranium-contaminated aquifer. *Appl. Environ. Microbiol.* **2003**, *69* (10), 5884−5891.
(77) Liu, C.; Shi, Z.; Zachara, J. M. Kinetics of uranium(VI) desorption from contaminated sediments: Effect of geochemical conditions and model evaluation. *Environ. Sci. Technol.* **2009**, *43* (17), 6560−6566.
(78) Neiss, J.; Stewart, B. D.; Nico, P. S.; Fendorf, S. Speciation-dependent microbial reduction of uranium within iron-coated sands. *Environ. Sci. Technol.* **2007**, *41* (21), 7343−7348.
(79) Dentz, M.; Le Borgne, T.; Englert, A.; Bijeljic, B. Mixing, spreading and reaction in heterogeneous media: A brief review. *J. Contam. Hydrol.* **2011**, *120−21*, 1−17.
(80) Cirpka, O. A.; Valocchi, A. J. Two-dimensional concentration distribution for mixing-controlled bioreactive transport in steady state. *Adv. Water Resourc.* **2007**, *30* (6−7), 1668−1679.
(81) Rolle, M.; Eberhardt, C.; Chiogna, G.; Cirpka, O. A.; Grathwohl, P. Enhancement of dilution and transverse reactive mixing in porous media: Experiments and model-based interpretation. *J. Contam. Hydrol.* **2009**, *110* (3−4), 130−142.
(82) Li, L.; Salehikhoo, F.; Brantley, S. L.; Heidari, P. Spatial zonation limits magnesite dissolution in porous media. *Geochim. Cosmochim. Acta* **2014**, *126* (0), 555−573.
(83) White, A. F.; Brantley, S. L. The effect of time on the weathering of silicate minerals: why do weathering rates differ in the laboratory and field? *Chem. Geol.* **2003**, *202* (3−4), 479−506.
(84) Salehikhoo, F.; Li, L.; Brantley, S. L. Magnesite dissolution rates at different spatial scales: The role of mineral spatial distribution and flow velocity. *Geochim. Cosmochim. Acta* **2013**, *108* (0), 91−106.
(85) Navarre-Sitchler, A.; Brantley, S. Basalt weathering across scales. *Earth Planet. Sci. Lett.* **2007**, *261* (1), 321−334.
(86) Chandler, D. P.; Knickerbocker, C.; Bryant, L.; Golova, J.; Wiles, C.; Williams, K. H.; Peacock, A. D.; Long, P. E. Profiling In Situ Microbial Community Structure with an Amplification Microarray. *Appl. Environ. Microbiol.* **2013**, *79* (3), 799−807.